The Astronomical Journal, 142:32 (11pp), 2011 July doi:10.1088/0004-6256/142/1/32

CYANOACETYLENE IN IC 342: AN EVOLVING DENSE GAS COMPONENT WITH STARBURST AGE*

David S. Meier[1,2,5], Jean L. Turner[3], and Eva Schinnerer[4]
[1] New Mexico Institute of Mining and Technology, 802 Leroy Place, Socorro, NM 87801, USA; dmeier@nmt.edu
[2] National Radio Astronomy Observatory, P.O. Box O, 1003 Lopezville Road, Socorro, NM 87801, USA
[3] Department of Physics and Astronomy, UCLA, Los Angeles, CA 90095-1562, USA; turner@astro.ucla.edu
[4] Max-Planck-Institut für Astronomie, Königstuhl 17, D-69117 Heidelberg, Germany; schinner@mpia.de
Received 2010 December 28; accepted 2011 May 4; published 2011 June 14

ABSTRACT

We present the first images of the $J = 5$–4 and $J = 16$–15 lines of the dense gas tracer, cyanoacetylene, HC_3N, in an external galaxy. The central 200 pc of the nearby star-forming spiral galaxy, IC 342, was mapped using the Very Large Array and the Plateau de Bure Interferometer. HC_3N(5–4) line emission is found across the nuclear mini-spiral, but is very weak toward the starburst site, the location of the strongest mid-IR and radio emission. The $J = 16$–15 and 10–9 lines are also faint near the large H II region complex, but are brighter relative to the 5–4 line, consistent with higher excitation. The brightest HC_3N emission is located in the northern arm of the nuclear mini-spiral, 100 pc away from the radio/IR source to the southwest of the nucleus. This location appears less affected by ultraviolet radiation and may represent a more embedded, earlier stage of star formation. HC_3N excitation temperatures are consistent with those determined from $C^{18}O$; the gas is dense 10^4–10^5 cm^{-3} and cool, $T_k < 40$ K. So as to not violate limits on the total H_2 mass determined from $C^{18}O$, at least two dense components are required to model IC 342's giant molecular clouds. These observations suggest that HC_3N(5–4) is an excellent probe of the dense, quiescent gas in galaxies. The high excitation combined with faint emission toward the dense molecular gas at the starburst indicates that it currently lacks large masses of very dense gas. We propose a scenario where the starburst is being caught in the act of dispersing or destroying its dense gas in the presence of the large H II region. This explains the high star formation efficiency seen in the dense component. The little remaining dense gas appears to be in pressure equilibrium with the starburst H II region.

Key words: galaxies: individual (IC 342) – galaxies: ISM – galaxies: starburst – radio lines: galaxies

1. INTRODUCTION

Little is known about the properties of the dense gas component on giant molecular cloud (GMC) scales in external galaxies yet it is dense gas ($n_{H_2} > 10^4$ cm^{-3}) that most directly correlates with global star formation rates (SFRs; e.g., Gao & Solomon 2004; Wu et al. 2005). To understand the evolution and regulation of current star formation in galaxies, dense gas properties need to be accurately characterized.

In a recent imaging survey of millimeter-wave molecular lines in the nearby spiral nucleus of IC 342, a surprising degree of morphological variation is observed in its dense gas (Meier & Turner 2005), which was not anticipated from CO or HCN (e.g., Ishizuki et al. 1990; Downes et al. 1992). These and other observations (e.g., García-Burillo et al. 2000, 2001, 2002; Usero et al. 2004, 2006) confirm that CO and HCN fail to fully constrain excitation and chemical properties of the dense clouds. Various probes of the dense component exist, each with various strengths and weaknesses (e.g., Meier & Turner 2005; Papadopoulos 2007; Bussmann et al. 2008; Narayanan et al. 2008; Krips et al. 2008; Graciá-Carpio et al. 2008). HCN(1–0) is the most commonly used dense gas tracer, primarily because it is bright, however, it is optically thick in most starburst environments (e.g., Downes et al. 1992; Meier & Turner 2004; Knudsen et al. 2007), has a widely spaced rotational ladder with its $J > 3$ transitions in the submillimeter and can be sensitive to chemical effects (photon-dominated region (PDR) effects and IR pumping; e.g., Fuente et al. 1993; Aalto et al. 2002).

Here, we present a study of the physical conditions of the very dense gas component of a nearby starburst nucleus using HC_3N. With its large electric dipole moment ($\mu = 3.72$ D versus 3.0 D for HCN), low opacity, and closely spaced rotational ladder accessible to powerful centimeter and millimeter-wave interferometers, HC_3N is well suited to high-resolution imaging of the structure and excitation of the densest component of the molecular gas (e.g., Morris et al. 1976; Vanden Bout et al. 1983; Mauersberger et al. 1990; Aladro et al. 2011). HC_3N(5–4) has a critical density of 5×10^4 cm^{-3} and an upper level energy of $E/k = 6.6$ K; the 16–15 line has a critical density of 5×10^5 cm^{-3} and an upper level energy of $E/k = 59$ K.

We have observed the $J = 5$–4 and $J = 16$–15 lines of HC_3N at $<2''$ resolution in IC 342 with the Very Large Array[6] (VLA) and the Plateau de Bure Interferometer, respectively. IC 342 is one of the closest ($D \sim 3$ Mpc or $2'' = 29$ pc; e.g., Saha et al. 2002; Karachentsev 2005), large spirals with active nuclear star formation (Becklin et al. 1980; Turner & Ho 1983). It is nearly face-on, with bright molecular line emission both in dense clouds and a diffuse medium (Lo et al. 1984; Ishizuki et al. 1990; Downes et al. 1992; Turner & Hurt 1992). The wealth of data and proximity of IC 342 permit the connection of cloud properties with star formation at sub-GMC spatial scales. The data published here represent the first high-resolution maps of HC_3N(5–4) and HC_3N(16–15) in an external galaxy. Excitation is a key component in the interpretation of molecular line intensities, so these two maps are compared with the previously published lower resolution HC_3N(10–9) map made with the Owens Valley Millimeter Array (Meier & Turner 2005), to

* Based on observations carried out with the IRAM Plateau de Bure Interferometer. IRAM is supported by INSU/CNRS (France), MPG (Germany), and IGN (Spain).
[5] Adjunct Assistant Astronomer.
[6] The National Radio Astronomy Observatory is a facility of the National Science Foundation operated under cooperative agreement with by Associated Universities, Inc.

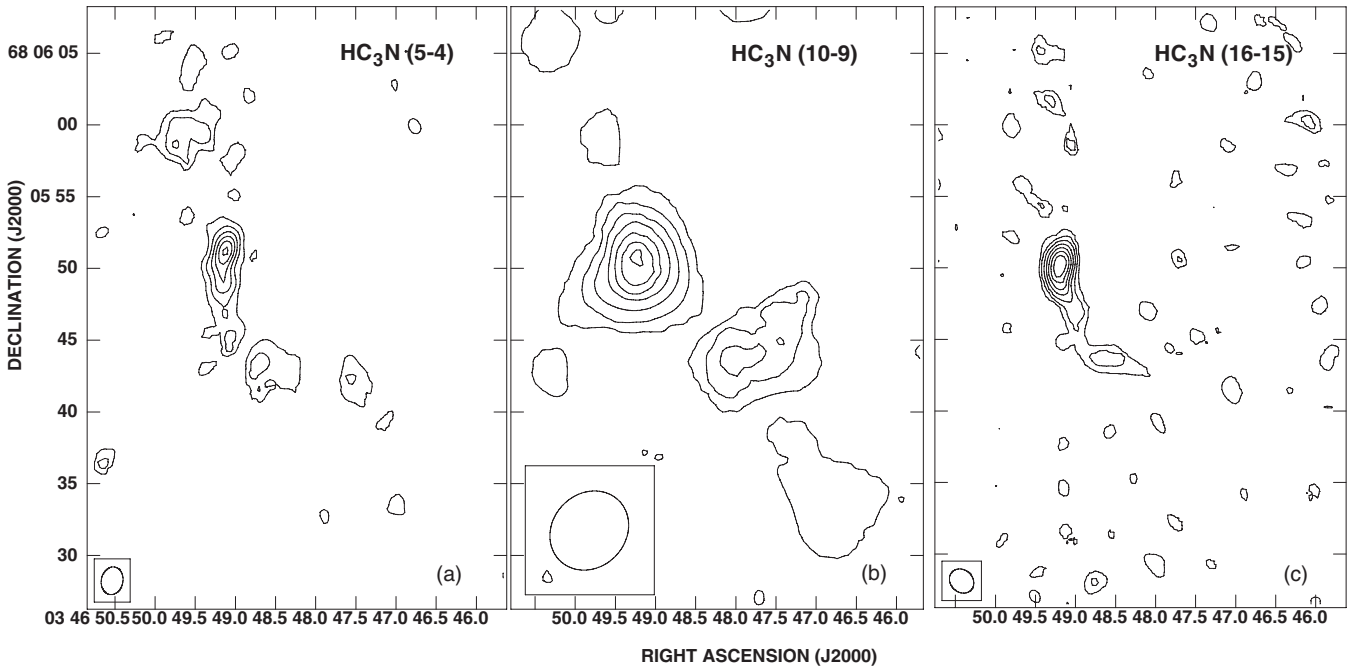

Figure 1. Continuum-subtracted HC_3N integrated intensity maps for IC 342. (a) The HC_3N(5–4) contoured in steps of 7.3 K km s^{-1} (3σ) for a resolution of $1\farcs95 \times 1\farcs50$. (b) A continuum-subtracted version of HC_3N(10–9) from Meier & Turner (2005) contoured in steps of 1.25 K km s^{-1} for a beam size of $5\farcs9 \times 5\farcs1$. (c) HC_3N(16–15) contoured in 3σ steps of 5.1 K km s^{-1} for a resolution of $1\farcs83 \times 1\farcs55$.

constrain the physical conditions of the densest component of the interstellar medium (ISM) in the center of IC 342 and to correlate properties of the dense gas with star formation, diffuse gas, and chemistry.

2. OBSERVATIONS

Aperture synthesis observations of the HC_3N $J = 5$–4 rotational line (45.490316 GHz) toward IC 342 were made with the D configuration of the VLA on 2005 November 25 (VLA ID: AM839). The synthesized beam is $1\farcs95 \times 1\farcs5$ (FWHM); position angle (P.A.) $= -11\fdg2$. Fifteen 1.5625 MHz channels were used, for a velocity resolution of 10.3 km s^{-1}, centered at $v_{\rm LSR} = 30$ km s^{-1}. The phase center is α(J2000) $= 03^{\rm h}46^{\rm m}48\fs3$; δ(J2000) $= 68\arcdeg05\arcmin47\farcs0$. Amplitude tracking and pointing was done by observing the quasar 0228+673 every 45 minutes. Phases were tracked by fast switching between the source and the quasar 0304+655 with 130 s/50 s cycles. Absolute flux calibration was done using 3C48 and 3C147 and is good to ∼5%–10%. Calibration and analysis was performed with the NRAO Astronomical Image Processing Software package. The naturally weighted and CLEANed data cube has an rms of 0.70 mJy beam^{-1}. Correction for the primary beam (∼1′ at 45 GHz) has not been applied. The shortest baselines in the data set are ≃5 kλ, corresponding to scales of ∼40″; structures larger than this are not well sampled.

The HC_3N(16–15) line emission in the center of IC 342 was observed with five antennas using the new 2 mm receivers of the IRAM Plateau de Bure interferometer (PdBI) on 2007 December 28 and 31 in C configuration with baselines ranging from 24 to 176 m. The phase center of the observations was set to α(J2000) $= 03^{\rm h}46^{\rm m}48\fs105$; δ(J2000) $= 68\arcdeg05\arcmin47\farcs84$. NRAO 150 and 0212+735 served as phase calibrators and were observed every 20 minutes. Flux calibrators were 3C84 and 3C454.3. The calibration was done in the GILDAS package following standard procedures. The HC_3N(16–15) line at 145.560951 GHz was observed assuming a systemic velocity of $v_{\rm LSR} = 46$ km s^{-1} and a spectral resolution of 2.5 MHz (5.15 km s^{-1}). The average 2 mm continuum was obtained by averaging line-free channels blue and redward of the HC_3N and H_2CO lines and subtracted from the uv data cube to obtain a continuum-free data cube. The final naturally weighted and CLEANed data cube with 10 km s^{-1} wide channels has a CLEAN beam of $1\farcs83 \times 1\farcs55$, P.A. $= 46\arcdeg$, and an rms of 1.7 mJy beam^{-1}.

Single-dish observations of HC_3N(16–15) find a peak brightness temperature of 6.7 mK in a 16″.9 beam (Aladro et al. 2011). Convolving our map to this beam and sampling it at the same location yields a peak brightness of 7.1 mK, which agrees within the uncertainties of both data sets. Therefore, no flux is resolved out of the interferometer maps, as expected for these high-density tracers.

3. RESULTS

3.1. The Dense Cloud Morphology

Continuum-subtracted integrated intensity line maps of HC_3N(5–4), HC_3N(10–9), and HC_3N(16–15) in IC 342 are shown in Figure 1. Figure 2 shows the 5–4 transition overlaid on the 7 mm continuum image generated from off-line channels. Locations of GMC cores (Downes et al. 1992; Meier & Turner 2001) and the optical clusters (e.g., Schinnerer et al. 2003), compared with HC_3N(5–4) and HCN(1–0) (Downes et al. 1992), are also shown in Figure 2. Figure 3 shows the HC_3N(5–4) and HC_3N(16–15) spectra (in flux units) taken over the same 2″ aperture centered on each cloud.

HC_3N(5–4) emission picks out most clouds seen in other dense gas tracers (e.g., HCN(1–0)). The only labeled cloud not clearly detected in HC_3N(5–4) is GMC B, the cloud associated with the nuclear star-forming region ($L_{\rm IR} \sim 10^8\ L_\odot$; Becklin et al. 1980; Turner & Ho 1983). Positions of the GMCs measured in HC_3N are consistent with those fitted in $C^{18}O$(2–1) to within

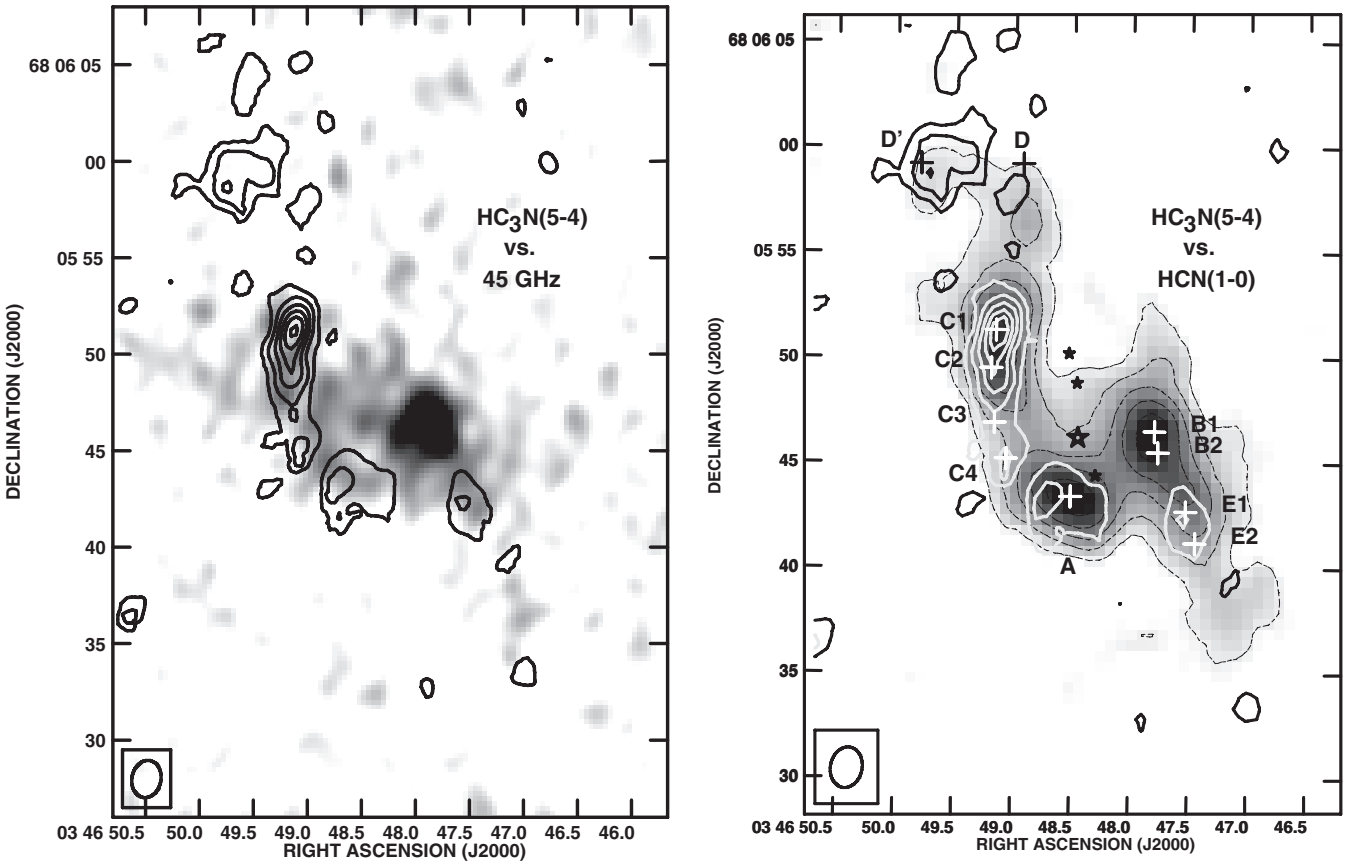

Figure 2. (a) The HC_3N(5–4) integrated intensity map (black line) for IC 342 overlaid on the 7 mm continuum emission (gray scale) extracted from the line-free portion of the HC_3N(5–4) data cube. The continuum gray scale ranges from 0.22 mJy beam^{-1} to 2.2 mJy beam^{-1}. HC_3N contours are as in Figure 1. (b) The HC_3(5–4) integrated intensity map overlaid on the HCN(1–0) emission (gray scale and dashed contours; Downes et al. 1992). HC_3N contours are as in (a). The HCN(1–0) gray scale runs from 0.50 Jy beam km s^{-1} to 4 Jy beam km s^{-1} and contours are in steps of 0.75 Jy beam km s^{-1}. Positions of GMC cores (Meier & Turner 2001) and optical clusters (e.g., Schinnerer et al. 2003, with absolute optical positions having absolute uncertainties of $\sim$1″) are labeled.

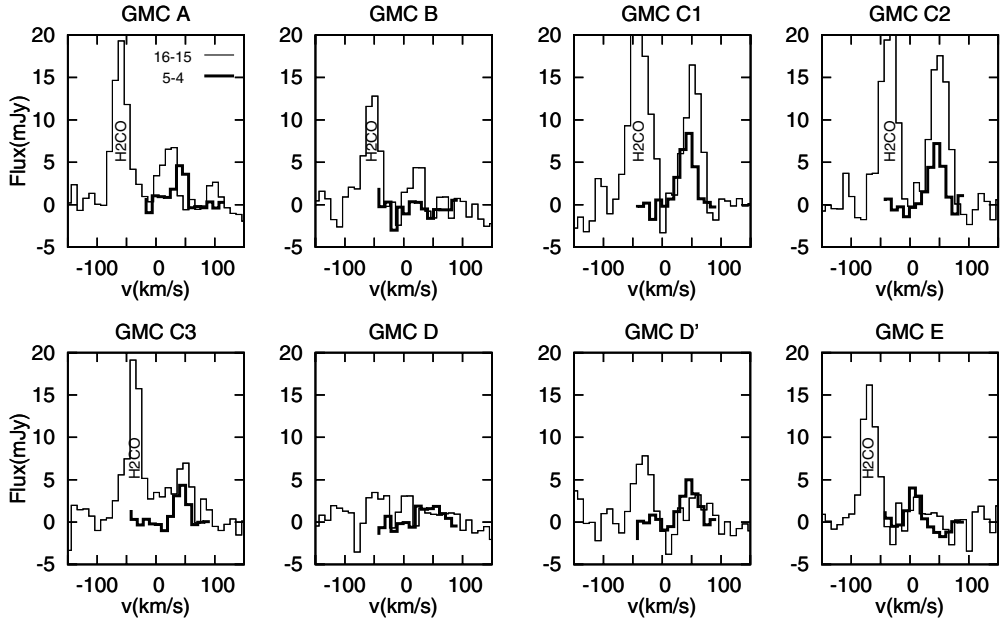

Figure 3. HC_3N(16–15) (thin line) and HC_3N(5–4) (thick line) spectra. Spectra are summed over 2″ apertures centered on each position at the locations of the main GMCs. Note that the bright spectral feature at ~ -60 km s^{-1} is $H_2CO(2_{02} - 1_{01})$.

a beam (Meier & Turner 2001). An additional GMC is detected in HC_3N(5–4) just south of GMC C3, labeled C4. Unlike $C^{18}O$(2–1) which peaks at GMC C2, HC_3N(5–4) emission peaks farther north, toward GMC C1, at a distance of 105 pc from the nucleus suggesting changes in excitation across GMC C. GMCs A and D′ are resolved into two components, but we do

Table 1
HC_3N Measurements

GMC	I(5–4)[a] (K km s^{-1})	S_{pk}(5–4) (mJy)	v_o(5–4) (km s^{-1})	Δv(5–4) (km s^{-1})	I(16–15)[a] (K km s^{-1})	S_{pk}(16–15) (mJy)	v_o(16–15) (km s^{-1})	Δv(16–15) (km s^{-1})
A	13 ± 2.6	5.0 ± 0.7	22 ± 2	29 ± 5	2.4 ± 0.5	7.0 ± 1.3	16 ± 3	44 ± 10
B	<5.3	<1.0	...	...	2.4 ± 0.5	5.2 ± 1.5	19 ± 3	28 ± 10
C1	44 ± 2.6	6.6 ± 0.5	48 ± 1	39 ± 3	8.5 ± 0.5	13 ± 1.1	47 ± 1	43 ± 4
C2	28 ± 2.6	5.7 ± 0.5	50 ± 1	35 ± 4	10 ± 0.5	19 ± 1.2	45 ± 1	47 ± 4
C3	14 ± 2.6	3.6 ± 0.5	49 ± 1	31 ± 5	2.8 ± 0.5	15 ± 1.0	45 ± 1	47 ± 4
D	13 ± 2.6	1.5 ± 0.5	51 ± 6	58 ± 20	<1.0	<2.5	...	...
D′	20 ± 2.6	3.8 ± 0.5	52 ± 2	40 ± 7	$\lesssim 1.0$	2.3 ± 1.1	57 ± 8	44 ± 26
E	14 ± 2.6	4.4 ± 1	12 ± 2	28 ± 7	<1.0	<2.5	...	...

Notes. Based on spectra from 2″ apertures centered on each cloud, except where noted. Uncertainties in the temperatures and intensities are the larger of the rms or 10% absolute calibration uncertainties. Uncertainties for the line centroids and widths are the 1σ uncertainties in the Gaussian fits.
[a] Based on the full resolution data.

Table 2
Line Ratios and Excitation

GMC	$R_{10/5}$[a]	$^{10/5}T_{ex}$[a] (K)	$R_{16/5}$[b]	$^{16/5}T_{ex}$[b] (K)	$C^{18}O\,T_{ex}$[c] (K)	$N(H_2)$[c] (cm^{-2})	$X(HC_3N)$	$C^{18}O\,M_{H2}$[c] ($M_\odot$)
A	0.55 ± 0.2	8.8 ± 1.5	0.14 ± 0.03	12 ± 0.6	13 ± 4	4(22)	1(−9)	4.4(5)
B	2.5 ± 1	37 ± 19	$\gtrsim 0.52$	$\gtrsim 18$	19 ± 8	4(22)	>8(−10)	7.6(5)
C1	0.80 ± 0.1	11 ± 1.0	0.20 ± 0.03	13 ± 0.6	8 ± 3[d]	7(22)	3(−9)	6.8(5)
C2	1.1 ± 0.1	14 ± 1.0	0.33 ± 0.03	15 ± 0.6	8 ± 3	1(23)	2(−9)	1.0(6)
C3	1.0 ± 0.1	13 ± 1.3	0.42 ± 0.07	17 ± 1.3	8 ± 3[d]	5(22)	1(−9)	4.9(5)
D	$\lesssim 0.15$	~ 5	<0.17	<13	6 ± 4	2(22)	3(−9)	6.4(5)
D′	~ 0.24	~ 6	0.061 ± 0.04	10 ± 1.8	~ 6	6(22)	1(−9)	5.8(5)
E	1.1 ± 0.3	14 ± 3.1	<0.057	<10	7 ± 3	6(22)	1(−9)	1.1(6)

Notes. Based on spectra from 2″ apertures centered on each cloud, except where noted. Uncertainties in the temperatures and intensities are the larger of the rms or 10% absolute calibration uncertainties. Uncertainties for the line centroids and widths are the 1σ uncertainties in the Gaussian fits.
[a] Based on 6″ data.
[b] Based on the full resolution data.
[c] From Meier & Turner (2001).
[d] Assumed to be constant across GMC C.

not discuss them as separate entities given the lower signal-to-noise, other than to state that there is a clear difference in velocity centroid between the 5–4 and 16–15 transitions (e.g., Figure 3) indicating there is likely an excitation gradient across GMC A. No emission $>2\sigma$ is detected toward the weak CO(2–1) feature associated with the central nuclear star cluster (Schinnerer et al. 2003).

The $J = 16$–15 line intensity is comparable to that of $J = 5$–4 line in all clouds. While dominated by GMC C, HC_3N(16–15) is detected (or tentatively detected) toward all clouds, except GMC D. Fluxes for GMCs D and D′ are quite uncertain since they are just inside the half power point of the PdBI primary beam. That GMC C is much brighter than the other clouds in both transitions indicates that large quantities of dense gas are present in this cloud. HC_3N(16–15) favors C2 over C1. GMC B, while still faint in an absolute sense, is significantly brighter in HC_3N(16–15) relative to 5–4. This is not unexpected given the higher excitation requirements of the 16–15 line and that both B and C2 have 7 mm continuum sources associated with massive star formation.

3.2. Gas Excitation and the HC_3N ΔJ Line Ratios

Comparisons of the HC_3N (5–4), (10–9), and (16–15) maps provide a chance to establish the excitation of the densest molecular cloud gas component. Line intensities from the $J = 5$–4 and $J = 16$–15 lines were measured over 2″ apertures centered on each of the GMCs. Table 1 records Gaussian fits to each spectrum along with integrated line intensities. Peak antenna temperature ratios are calculated for HC_3N(16–15)/HC_3N(5–4), hereafter denoted $R_{16/5}$. $R_{16/5}$ ranges from less than 0.06 up to ∼0.5, with GMC B having the highest value (Table 2). The 5–4 and 16–15 transitions generally bracket the peak of the level populations, so we achieve good constraints on gas excitation. LTE excitation temperatures, T_{ex}, implied by $R_{16/5}$ range from <10 K to >18 K (where we have neglected T_{cmb} in this determination). Excitation is lowest toward GMCs D, D′, and E. These excitation temperatures T_{ex} are similar to those found from the presumably much less dense gas traced in $C^{18}O$ (Table 2; Meier & Turner 2001). Only the GMC C clouds have significantly higher T_{ex} in HC_3N—toward C1–C3 $T_{ex}(HC_3N)$ are about a factor of two greater than $T_{ex}(C^{18}O)$.

The resolution of the HC_3N(10–9) data is significantly lower than it is for the 5–4 and 16–15 lines. To compare $J = 5$–4 and $J = 10$–9 line intensities, the 5–4 data were convolved to the resolution of the (10–9) data (5.″9 × 5.″1; Meier & Turner 2001), then integrated intensity ratios, hereafter $R_{10/5}$, were sampled at the locations of $R_{16/5}$. Though at lower resolution than $R_{16/5}$, we make the approximation that $R_{10/5}$ does not change on these sub-GMC scales. While leading to larger uncertainties, this provides a way to include all three transitions in modeling dense gas

excitation at very high resolution. $R_{10/5}$ range from 0.25 to 1.4 (Table 1). GMC B has the highest value of 1.4. The remainder of the GMCs have ratios of $0.3 < R_{10/5} < 0.6$. Excitation temperatures implied by these ratios range from $T_{ex} =$ 6–16 K, consistent with those derived from $R_{16/5}$ separately. T_{ex} derived from $R_{10/5}$ are similar to those derived from $C^{18}O$. The only exception here is GMC A, the cloud where PDRs dominate (Meier & Turner 2005). Toward GMC A $T_{ex}(C^{18}O)$ and $T_{ex}(R_{16/5})$ are 12–13 K, twice that of $T_{ex}(R_{10/5})$.

Before modeling the densities implied by the line ratios, we test whether IR pumping can be responsible for the observed excitation. IR pumping is important if

$$^{vib}B_{ul}\,I_\nu(45\,\mu m) \gtrsim {}^{rot}A_{ul}, \quad (1)$$

where $^{vib}B_{ul}$ is the Einstein B_{ul} of the corresponding $v_7 = 1$ vibrational transitions at ~45 μm, $I_\nu(45\,\mu m)$ is the 45 μm intensity as seen by the HC_3N molecules, and $^{rot}A_{ul}$ is the Einstein A_{ul} of the rotational state (e.g., Costagliola & Aalto 2010). It is extremely difficult to estimate the applicable 45 μm IR intensity, but it is expected to be most intense toward the starburst GMC (B). A detailed assessment of IR pumping must await high-resolution MIR maps, but we constrain $I_\nu(45\,\mu m)$ in several ways. First, we take the 45 μm flux from Brandl et al. (2006) and scale it by the fraction of total 20 μm flux that comes from within 2.″1 of the starburst as found by Becklin et al. (1980) and then average over that aperture. For the average $I_\nu(45\,\mu m)$ calculated this way, $^{vib}B_{ul}\,I_\nu(45\,\mu m)$ is 10^{-4} ($10^{-2.5}$) times too low to pump the 16–15 (5–4) transition. Alternatively, if we (very conservatively) take the total MIR luminosity from the central 30″ and assume that it comes from a blackbody of the observed color temperature (e.g., ~50 K; Becklin et al. 1980) then $I_\nu(45\,\mu m)$ is still at least an order of magnitude too low to meet the inequality in Equation (1) for both transition. IR pumping rates only become comparable to $^{rot}A_{ul}$ for the 5–4 transition if the total IR luminosity originates from a ~2.5 pc source with a source temperature of $\gtrsim$100 K. We conclude that IR pumping is not important for the 16–15 transition of HC_3N in any reasonable geometry of the IR field. For the 5–4 transition to be sensitive to IR pumping, the IR source must be warm, opaque, and extremely compact. Therefore, IR pumping is neglected for all clouds in the following discussion.

3.3. Physical Conditions of IC 342's Dense Gas—LVG Modeling

The values of the excitation temperature constrain the density and kinetic temperatures, n_{H_2} and T_k, and the physical conditions of the clouds driving the excitation. A series of large velocity gradient (LVG) radiative transfer models were run to predict the observed intensities and line ratios for a given n_{H_2}, T_k, and filling factor, $f_a = \Omega_{source}/\Omega_{beam}$, of the dense component (e.g., Vanden Bout et al. 1983). Single-component LVG models are instructive, particularly when lines are optically thin, as is the case for HC_3N. The LVG model used is that of Meier et al. (2000), adapted to HC_3N, with levels up to $J = 20$ included. Collision coefficients are from Green & Chapman (1978). A range of densities, $n_{H_2} = 10^2$–10^6 cm^{-3}, and kinetic temperatures, $T_k =$ 0–100 K, was explored. HC_3N column densities based on LTE excitation (Table 2) are calculated at 2″ resolution from

$$N_{mol} = \left(\frac{3kQe^{E_u/kT_{ex}}}{8\pi^3\nu S_{ul}\mu_0^2 g_{K_u} g_{I_u}}\right) I_{mol}, \quad (2)$$

using molecular data of Lafferty & Lovas (1978), HC_3N(5–4) intensities, and $T_{ex}(HC_3N)$ from Table 2. HC_3N abundances are found to be $X(HC_3N) \simeq 10^{-9.1}$–$10^{-8.5}$, with the highest values toward C1 and D. While uncertain these abundances agree with those found in Meier & Turner (2005) and are typical of Galactic center HC_3N abundances (e.g., Morris et al. 1976; de Vicente et al. 2000) and good enough for constraining $X/dv/dr$. The ratio of cloud line width to core size is ~1–3 km s^{-1} pc^{-1} for the GMCs. Therefore, we adopt a standard model abundance per velocity gradient of $X/dv/dr = 10^{-9}$ km s^{-1}, but run models for values of $X/dv/dr$=10^{-11}–10^{-9}.

Antenna temperatures are sensitive to the unknown filling factor. In these extragalactic observations, the beam corresponds to scales large compared to cloud structure, and hence filling factors are not directly known. To first order, the line ratios, $R_{10/5}$ and $R_{16/5}$, are independent of filling factor if we assume that HC_3N(5–4), (10–9), and (16–15) originate in the same gas. So model ratios are compared to the observed data to constrain parameter space. For the parameter space implied by the line ratios model brightness temperatures are determined. A comparison of the model brightness temperature to the observed brightness temperature sets the required areal filling factors for that solution.

3.3.1. Physical Conditions of the Dense Component

Figure 4 displays the results of the LVG modeling. Acceptable $\pm1\sigma$ (T_k,n_{H_2}) parameter spaces are shown for each line ratio ($R_{10/5}$, thick solid gray line; $R_{16/5}$, thick solid black line). Also shown in Figure 4 are the acceptable solutions obtained from the $C^{18}O$(2–1)/$C^{18}O$(1–0) line ratio (thin gray lines; Meier & Turner 2001). Figure 5 and Table 3 display the model flux versus upper J state of the line for the $T_K = 10$ K, 30 K, and 50 K solutions (also 70 K solutions for GMC B).

HC_3N(5–4) has a critical density of $n_{cr} \sim 5 \times 10^4$ cm^{-3} and an upper energy state of 6.55 K. HC_3N(16–15) has a critical density, $n_{cr} \sim 5 \times 10^5$ cm^{-3} and an upper energy state of 59 K. HC_3N(10–9) values are intermediate. Therefore, $R_{10/5}$ and $R_{16/5}$ are sensitive probes of n_{H_2} between the range of 10^4 and 10^6 cm^{-3}. Observed ratios constrain n_{H_2} to ~$\pm$0.1 dex at a given T_k and to ~$\pm$0.3 dex for all modeled $T_k > 20$ K. For $T_k \gtrsim 40$ K, ratios are largely insensitive to T_k (curves are horizontal). The LVG models do not constrain density when T_k is low. Thus, to narrow the range of possible solutions requires two or more line ratios, or an external constraint on one of the axes. Kinetic temperatures of the dense component at 2″ scales in IC 342 remain largely unconstrained to date. One method of constraining the kinetic temperature is the peak T_b at this resolution of the optically thick CO(2–1) line. Using this method, $T_k \simeq$ 35–45 K toward GMCs A, B, and C, and $T_k \simeq$ 15–20 K for GMCs D, D′, and E (Turner et al. 1993; Schinnerer et al. 2003). These values are not highly discordant from arcminute resolution $T_k \sim$ 50 K measurements from NH_3 (Ho et al. 1982) or the far-infrared dust temperature of 42–55 K (Becklin et al. 1980; Rickard & Harvey 1984). However, the CO(2–1) traces gas with densities two to three orders of magnitude lower than these HC_3N transitions, so it is not clear that this is the relevant T_k for the dense cores of the GMCs.

Valid solutions are found for the GMCs, with the exception of GMC D′, which is the most uncertain due to its distance from the center of the field. (No fit is attempted for GMC D because both HC_3N(5–4) and HC_3N(16–15) are upper limits or tentative detections.) The solutions show modest cloud excitations given

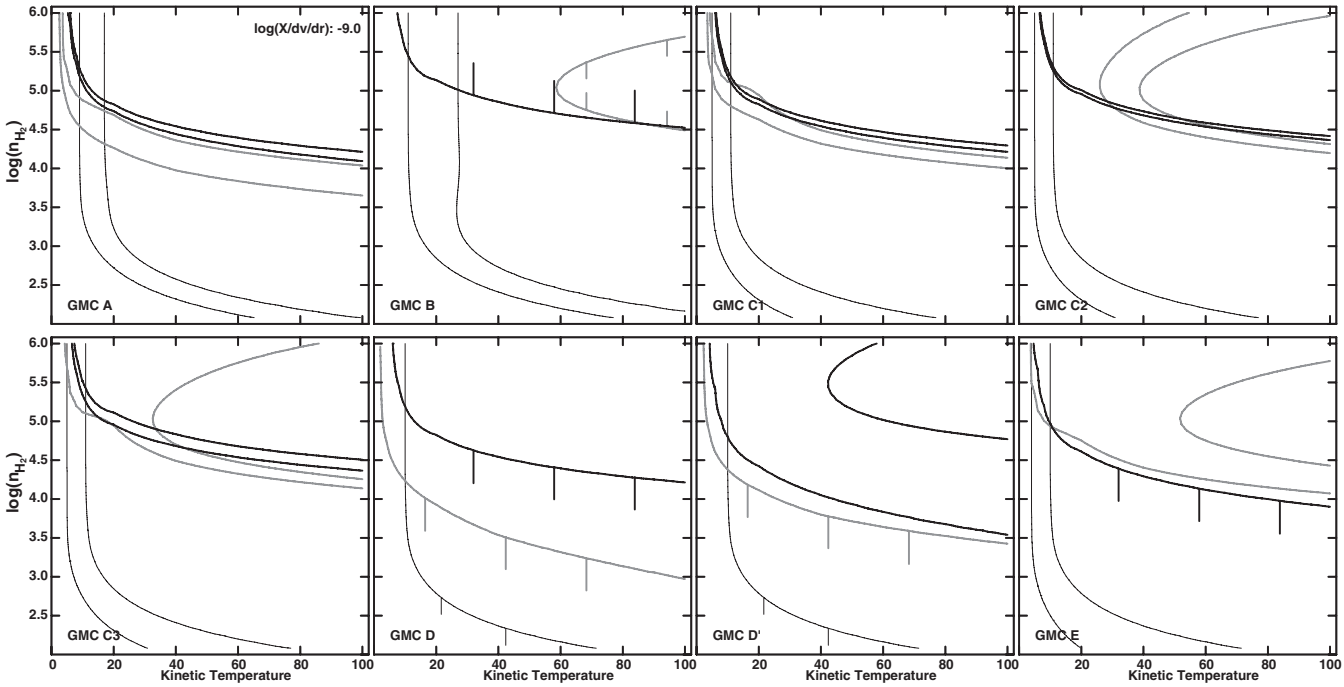

Figure 4. (a) The HC_3N LVG models of the GMCs in IC 342. The thick black lines delineate the observed $\pm 1\sigma$ range of the $HC_3N(16–15)/HC_3N(5–4)$ line ratio ($R_{16/5}$), sampled at 2″ resolution. The thick gray lines represent the observed $\pm 1\sigma$ range of the $HC_3N(10–9)/HC_3N(5–4)$ line ratio ($R_{10/5}$), sampled at 6″ resolution. $X(HC_3N)/dv/dr = 10^{-9}$ is assumed for the displayed models. The thin black lines display the $\pm 1\sigma$ range implied by LVG models of $C^{18}O$ for comparison (Meier & Turner 2001). Downward (upward) tick marks indicate upper (lower) limits.

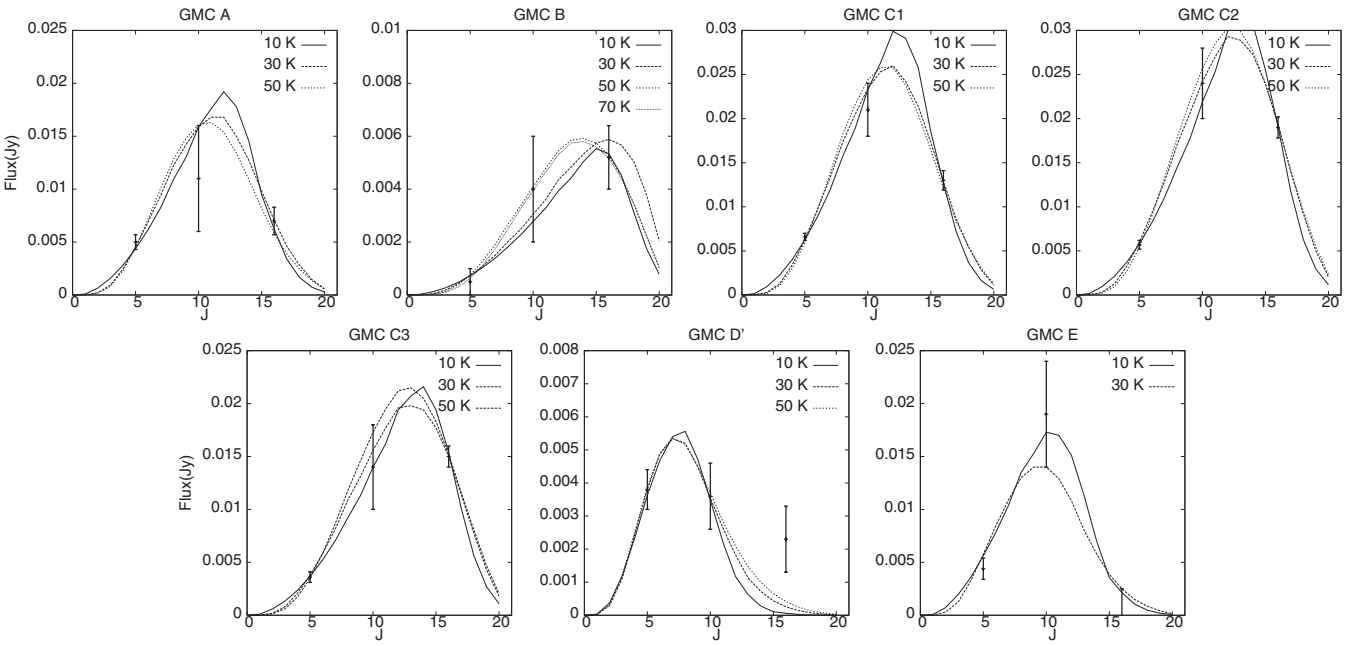

Figure 5. HC_3N level population diagrams. Fluxes are taken from a 2″ box centered on the emission peak. $HC_3N(10–9)$ fluxes are extrapolated from the (5–4) data using the line ratios in Table 1. For each GMC, fitted LVG solutions are displayed for $T_K = 10$ (solid lines), 30 (dashed lines), and 50 K (dotted lines), except GMC B which includes $T_K = 70$ K (dot-dashed lines) (Table 3). Only models with $X(HC_3N)/dv/dr = 10^{-9}$ km^{-1} s are shown.

the strong nuclear star formation. Good agreement is observed between solutions found using $R_{16/5}$ and $R_{10/5}$ when kinetic temperatures are low ($T_k < 30$ K). Given uncertainties in line intensities and $X(HC_3N)/dv/dr$, higher temperatures cannot be ruled out. While T_k itself is less well constrained, the combination $n_{H_2}T_k$ is well determined. Since line brightnesses are the measured quantity, as gas temperatures are raised, densities or filling factors must decrease to compensate. The nature of the solutions are such that the densities decrease more than the filling factors (Table 4).

GMCs A, C1, and C3 are best fit with $n_{H_2} \sim 10^{4.7}$–$10^{5.2}$ cm^{-3} and $T_k \simeq 20$ K. For $T_k = 50$ K derived densities drop to $n_{H_2} \sim 10^{4.3}$–$10^{4.7}$ cm^{-3}, while they drop to $n_{H_2} \sim 10^{3.7}$–$10^{4.4}$ cm^{-3} for $T_k = 100$ K. Changes in $X/dv/dr$ do not strongly influence the derived solutions. Toward these clouds filling factors are $f_a \simeq 0.03$–0.1. For comparison, a 1 pc^2 cloud would have

Table 3
One-component HC_3N LVG Solutions ($X/dv/dr = 10^{-9}$)

GMC	T_k (K)	$\log(n_{H_2})$ ($\log(cm^{-3})$)	f_a	$\frac{\sqrt{n_{H_2}}}{T_k}$	M_{den}[a] ($M_\odot$)	$\frac{M_{den}}{M_{H_2}}$	$\log(n_{H_2} T_k)$ ($\log(cm^{-3}$ K))
A	10	5.15	0.091	38	4.7(6)[b]	11	6.16
	30	4.63	0.051	6.9	6.0(5)	1.4	6.11
	50	4.39	0.067	3.1	5.2(5)	1.2	6.09
B	10	5.75	0.015	75	1.3(6)	1.7	6.75
	30	5.22	4.7(−3)	14	6.5(4)	0.084	6.70
	50	4.87	6.0(−3)	5.5	4.2(4)	0.055	6.57
	70	4.81	5.4(−3)	3.6	3.1(4)	0.041	6.66
C1	10	5.23	0.13	41	9.7(6)	14	6.23
	30	4.69	0.066	7.4	1.0(6)	1.5	6.17
	50	4.50	0.075	3.6	8.0(5)	1.2	6.19
C2	10	5.36	0.12	48	1.3(7)	13	6.36
	30	4.80	0.056	8.4	1.0(6)	1.0	6.28
	50	4.64	0.057	4.2	7.3(5)	0.73	6.34
C3	10	5.44	0.076	53	7.1(6)	14	6.44
	30	4.86	0.033	9.0	5.3(5)	1.1	6.34
	50	4.70	0.034	4.5	3.8(5)	0.0.76	6.40
D	10	<4.49	>0.040	...	...	...	<5.49
	30	<4.10	>0.040	...	...	...	<5.58
	50	<3.88	>0.060	...	...	...	<5.58
D′	10	...	...	...	...	...	...
	30	...	...	...	...	...	...
	50	...	...	...	...	...	...
E	10	4.90	0.12	28	4.0(6)	3.6	5.90
	30	4.36	0.096	5.1	8.3(5)	0.75	5.84
	50	...	...	...	...	...	...

Notes.
[a] M_{dense} is an estimate of the dense H_2 mass implied by these LVG solutions. $M_{den} = m_{H_2} n_{H_2} R_e^3$, with R_e defined as $R_e^2 = f_a A_{aper}$.
[b] Numbers of the form $a(b)$ are equal to $a \times 10^b$.

Table 4
Two-component HC_3N LVG Solutions ($X/dv/dr = 10^{-9}$)

GMC	both T_k (K)	$\log(n_\ell)$ ($\log(cm^{-3})$)	Γ	$\log(\tilde{n})$ ($\log(cm^{-3})$)	$\frac{\sqrt{\tilde{n}}}{T_k}$	$\frac{M_{den}}{M_{H_2}}$	$\frac{N_{Lyc}}{M_{den}}$ ($s^{-1}\ M_\odot^{-1}$)
A	30	2.6	0.015	3.01	1.1	0.62	4.0(45)
	50	2.4	0.017	2.82	0.55	0.63	4.0(45)
B	30	2.8	3.2(−4)	2.83	0.87	0.078	5.2(46)
	50	2.5	4.6(−4)	2.54	0.37	0.097	4.2(46)
	70	2.4	4.0(−4)	2.44	0.24	0.092	4.4(46)
C1	30	2.4	0.017	3.03	1.1	0.77	1.9(45)
	50	2.1	0.021	2.90	0.56	0.84	1.8(45)
C2	30	2.4	0.021	3.03	1.1	0.77	2.1(45)
	50	2.1	0.013	2.87	0.54	0.83	1.9(45)
C3	30	2.3	5.0(−3)	2.80	0.84	0.69	4.1(45)
	50	2.1	6.3(−3)	2.64	0.42	0.72	4.0(45)
D	30	<2.5	...	...	...	...	...
	50	<2.3	...	...	...	...	...
D′	30	...	...	...	...	...	...
	50	...	...	...	...	...	...
E	30	2.3	0.030	2.94	0.99	0.78	1.6(45)
	50	2.0	...	...	...	...	...

Notes. The low-density component comes from the LVG solutions to $C^{18}O$ (Meier & Turner 2001). For the sake of simplicity it is assumed that the kinetic temperature of both the low- and high-density components are the same. See section 4.2 for discussion of Γ and $\tilde{n}$.

$f_a \simeq 0.0012$ for the aperture size and IC 342's distance. Therefore, these GMCs appear to have a few dozen dense clumps similar to the larger clumps found in Galactic GMCs (e.g., Myers & Benson 1983; Zinchenko et al. 1998). GMC C2 appears to have similar densities but slightly elevated temperatures, $T_k \simeq 30$ K. In GMCs D and D′ densities are at least a factor of four lower than the other clouds. Little can be said about the kinetic temperatures of these GMCs. GMC D′ is the only location with

statistically discrepant solutions from $R_{10/5}$ and $R_{16/5}$. Here, the (16–15) line is somewhat brighter than would be expected from the $R_{10/5}$.

The starburst GMC, B, is markedly different from the others. The combination of a low absolute HC_3N brightness temperature and high ratios, $R_{10/5}$ and $R_{16/5}$, require higher densities of $n_{H_2} \gtrsim 10^5$ cm^{-3} and a smaller ($f_a < 0.02$) filling factor. Both line ratios seem to indicate a kinetic temperature of more than $T_k \simeq 40$ K, and perhaps significantly higher, averaged over our 30 pc beam. The dense gas in GMC B, which is closest to the active star-forming region and IR source, is more compact, denser, and more highly excited than the other clouds.

For our own Galactic center, it has long been argued that molecular clouds must be unusually dense, at least $n \sim 10^4$ cm^{-3} to withstand tidal forces (e.g., Stark et al. 1989). If one assumes that GMC C, the most well-defined cloud, is a point mass in a spherical mass potential of the galaxy, its Roche limit would be at a radius of 25 pc. The radius of the combined C1–C2–C3 complex is >25 pc. In IC 342, the proximity to the nucleus where the strong non-circular velocity field (Turner & Hurt 1992) together with feedback from the starburst (Schinnerer et al. 2008) suggests that these clumps have densities large enough to maintain their identity but likely will not remain gravitationally bound to each other.

3.3.2. Comparisons between HC_3N and $C^{18}O$ Physical Conditions

For all GMCs (including GMC B), $T_{ex}(HC_3N) \simeq T_{ex}(C^{18}O)$. If a model in which all the H_2 exists in one uniform component, then the similarity of T_{ex} from both HC_3N and $C^{18}O$ implies that the densities of the molecular clouds are high enough ($>10^{4.5}$ cm^{-3}) to thermalize both $C^{18}O$ and HC_3N across the nucleus. (LVG solutions for $C^{18}O$ $J = 2$–1 and 1–0 lines from Meier & Turner 2001 are shown with the HC_3N solutions in Figure 4.) In this monolithic model the low observed T_{ex} of 10–20 K demand that the thermalized clouds must be quite cool. These temperatures are similar to those of dark clouds in the disk of our Galaxy, which is somewhat surprising given the elevated SFR in the nucleus of IC 342.

However, this model of a monolithic, dense, cold ISM seen in both HC_3N and $C^{18}O$ runs into problems with total mass constraints. If the ISM is uniformly this dense and cold, then the total dense gas cloud mass implied by the required densities and filling factors becomes very large, greater than permitted based on the optically thin $C^{18}O$ line emission. In Table 3, the total mass of dense gas, M_{den}, is approximated from the LVG solutions assuming $M_{den} = m_{H_2} n_{H_2} R^3$, with R defined as $R = \sqrt{f_a A_{beam}}$. Table 2 lists the total molecular gas mass, M_{H_2}, estimated from $C^{18}O$(2–1) data (see Meier & Turner 2001) assuming $M_{H_2} = m_{H_2} N_{H_2} A_{beam}$. One can see that M_{den} is typically larger than M_{H_2} for $T_k < 30$ K and diverges rapidly as T_k drops toward the LVG-favored values. In short if GMCs have uniformly such high densities and cold temperatures, then the clouds would contain too much H_2 mass for what is observed in $C^{18}O$. To match the line ratios while not violating mass constraints requires a multi-component dense ISM. A possible two-component model of the dense gas is discussed in Section 4.2.

4. DENSE GAS AND THE CO CONVERSION FACTOR

A consideration of the conversion factor between CO intensity and H_2 column density, X_{CO}, in the nuclear region of IC 342 suggests that the model of a single, high-density, and relatively cool ISM is not consistent with observations of CO isotopologues. Moreover, these clouds are unlikely to resemble Galactic disk GMCs in their internal structure and dynamics.

4.1. The Single-component Model and X_{CO}

The well-known Galactic relation between CO intensity and H_2 column density, $X_{CO} = I_{CO}/N(H_2)$, can be explained if GMCs consist of optically thick (in CO) turbulent clumps in virial equilibrium (e.g., Larson 1981; Solomon et al. 1987; Scoville & Sanders 1987). For the clumps to emit in HC_3N densities must be large enough so that T_b can legitimately be approximated by T_k. If we adopt this model, then X_{CO} is approximated by

$$X_{CO} \simeq 0.84 \times 10^{20} \left[\frac{\sqrt{\phi\, {}^{cl}n}}{f_a^{cl} T_k} \right] \text{cm}^{-2}\,(\text{K km s}^{-1})^{-1}, \quad (3)$$

where ϕ is the volume filling factor and ${}^{cl}n$ is the density of the clumps (Sakamoto 1996; Maloney & Black 1988). From the brightness of the CO isotopic lines, ${}^{CO}f_a \sim 1$ on 2″ scales (Meier & Turner 2001). The conversion factor X_{CO} within the central few hundred pc of IC 342 has been determined to be 0.6×10^{20} cm^{-2} (K km s^{-1})$^{-1}$ (Meier & Turner 2001). If the monolithic model presented in the previous section is correct and clouds are virialized clumps in equilibrium, then $\sqrt{{}^{cl}n}/T_k$ must be $\lesssim 0.75$ to match the observed conversion factor.

Table 3 records $\sqrt{{}^{cl}n}/T_k$ for each of the LVG solutions across the nucleus of IC 342. For all solutions, $\sqrt{{}^{cl}n}/T_k$ is greater than the required value, especially at low T_k. For the single-component, LVG favored T_k of ~10–20 K toward the more quiescent clouds, $\sqrt{{}^{cl}n}/T_k$ ~5–75, implying ${}^{IC342}X_{CO}$ should be several times larger than ${}^{MW}X_{CO}$. However, X_{CO} in the nucleus of IC 342 is 3–4 times *lower* than the Galactic conversion factor, based on both optically thin isotopologues of CO as well as dust emission (Meier & Turner 2001). Lower conversion factors appear to be the norm for the nuclei of gas-rich star-forming galaxies, including our own (e.g., Smith et al. 1991; Scoville et al. 1997; Dahmen et al. 1998; Harrison et al. 1999; Meier & Turner 2004; Meier et al. 2008). In the nuclear region of IC 342, dense gas kinetic temperatures do not appear to be higher than the Galactic disk value by an amount large enough to offset the observed increase in density over typical Galactic disk-like clouds; $T_k > 100$ K would be required. Recently, Wall (2007) completed a more generalized treatment of the conversion factor including radiative transfer and concludes that the true exponential dependences of n_{H_2} and T_k are weaker than 0.5 and −1, respectively. However, in all cases modeled, the dependences remain positive for n_{H_2} and negative for T_k.

In summary, it is not possible to reconcile bright HC_3N emission from uniformly cool, dense gas (low T_k, high n_{H_2}, and high f_a) with the known total amount of H_2 present if virialized constant density clumps are adopted.

4.2. A Possible Two-component Model and X_{CO}

The lack of an apparent connection between $\sqrt{{}^{cl}n}/T_k$ of the dense component and the observed conversion factor indicates that the clouds in the nucleus of IC 342 cannot be treated as simple virialized collections of uniform density clumps. One might expect that a large fraction of the $C^{18}O$ emission could originate from a moderate density component that is distinct from the denser, HC_3N-emitting gas. (Note that ^{12}CO traces a

distinct component more diffuse than that traced both by $C^{18}O$ (Meier et al. 2000) and HC_3N.)

As a first-order extension to the basic virialized clump model, we imagine two spatially well-mixed sets of clumps; one low density $C^{18}O$ emitting, n_l, and one high density, n_h, that emits both $C^{18}O$ and HC_3N. Assuming that the fraction, by number, of clumps with high density is Γ, then if both clumps have the same T_k, the virialized clump X_{CO} relation becomes

$$^{2comp}X_{CO} \simeq 0.84 \times 10^{20} \left[\frac{\sqrt{\phi\tilde{n}}}{f_a T_k}\right] \mathrm{cm}^{-2}\,(\mathrm{K\,km\,s^{-1}})^{-1}, \quad (4)$$

where $\tilde{n} = (1-\Gamma)n_l + \Gamma n_h$. The ratio of dense gas to total H_2 becomes $M_{den}/M_{tot} \simeq \Gamma n_h/((1-\Gamma)n_l + \Gamma n_h) = \Gamma n_h/\tilde{n}$. For a given T_k, n_l is chosen to match the $C^{18}O$ LVG solution (Meier & Turner 2001), while n_h is chosen to match the HC_3N LVG solutions, and $\Gamma = \phi_{HC_3N}/\phi_{CO} \simeq f_a^{3/2}$. Table 4 displays the adopted $C^{18}O$ LVG solutions, along with the new $\sqrt{\tilde{n}}/T_k$ and M_{den}/M_{tot} for the two-component model, assuming, for simplicity, that T_k is the same for both components. $\sqrt{\tilde{n}}/T_k$ and hence X_{CO} are decreased from the simple one-component model by factors of at least four. This simple extension results in closer agreement between the observed and calculated values of X_{CO} (especially when including the somewhat super-virial line widths), while maintaining most of the mass in the dense (low filling factor) component.

It is almost certainly the case that this extension is an oversimplification. In reality, we expect the clouds to exhibit a continuum of densities. However, the LVG modeling demonstrates that at least these three components are required to match the multi-transition observations of ^{12}CO, ^{13}CO, $C^{18}O$, and HC_3N. This is consistent with conclusions from recent single-dish modeling of higher J transitions of HC_3N (Aladro et al. 2011), but we find that multiple components are required to match intensities not only between GMCs but within individual GMCs.

5. HC_3N-EMITTING DENSE GAS AND STAR FORMATION

5.1. HC_3N versus HCN(1–0)

HCN(1–0) emission is the workhorse for relating quantities of dense gas to star formation (e.g., Gao & Solomon 2004). It is interesting to compare conclusions about the dense component from HC_3N with those of the more commonly used HCN(1–0). HCN(1–0) has been mapped at similar spatial resolution by Downes et al. (1992). Figure 2 compares HC_3N(5–4) to HCN(1–0). While HC_3N generally traces the same dense GMCs seen in HCN, their relative brightnesses are rather different. In HCN(1–0), GMC A, B, and C are all within 10% of the same brightness and GMCs D and E are 100% and 50% weaker, respectively. Whereas in HC_3N(5–4) and (16–15), C dominates, B is nearly absent and A is not significantly different from D and E. Comparisons with HC_3N clearly demonstrate that there is larger variations in dense gas properties than HCN indicates. The dominate difference is enhanced HCN toward the starburst and GMC A relative to GMC C. Unlike the HC_3N transitions, HCN(1–0) is optically thick and has slightly larger (25%–50%) filling factors (Downes et al. 1992). As kinetic temperatures increase, optically thick transitions brighten more rapidly than (lower excitation) optically thin transitions. Hence, it is expected that the HCN emission should favor somewhat warmer dense gas. Likely this effect results in the much brighter relative HCN(1–0) intensities toward the starburst. The relative enhancement toward GMC A is less clear. However, this cloud is known to be dominated by PDRs (Meier & Turner 2005), strongly influenced by mechanical feedback from the nuclear cluster (Schinnerer et al. 2008) and has a complicated HC_3N temperature and velocity structure (Sections 3.1 and 3.2). This cloud must have a complex density and temperature structure, potentially with a warmer intermediate density medium (Table 2). Moreover, HCN abundances can be elevated in PDRs.

We conclude that HCN(1–0) does a good job locating the dense gas but it does a poorer job tracing small-scale variation in the properties of the dense gas when a mix of strong star formation and quiescent gas is present. It is expected that such effects should become more important as specific SFRs increase and spatial scales decrease.

5.2. HC_3N versus Star Formation

The brightest HC_3N emission and the brightest star-forming regions do not coincide. Most of the current star formation, traced by bright infrared and thermal radio continuum emission (Becklin et al. 1980; Turner & Ho 1983), is situated about 50 pc to the southwest of the dynamical center, in the vicinity of GMC B. The brightest HC_3N emission by far is on the northeast side of the nucleus, in the northern molecular arm centered at GMC C2. This region has free–free emission amounting to only a third of the brightness of the strongest radio source, associated with GMC B. The faintness, in absolute terms, of HC_3N(16–15) toward GMC B is unexpected and important reflecting a much lower areal filling of warm, very dense gas here. Either the number of cloud clumps or their size is small relative to the other GMCs.

On the other hand, the excitation of HC_3N does reflect the presence of young forming stars. HC_3N(16–15) and HC_3N(10–9) are relatively brighter toward the current starburst. This suggests that the absence of a correlation between HC_3N(5–4) intensity and star formation is partly due to depopulation of the lower energy transitions. GMCs that are faint in the HC_3N $J = 16$–15 transition and not associated with strong star formation show up well at the lower J transitions of HC_3N, as would be expected for gas of lower excitation. Clearly there is a large amount of dense gas currently not actively forming stars, that shows up in the low excitation transitions of HC_3N. This is consistent with the fact that both HNC(1–0) and N_2H^+(1–0), generally considered dense quiescent gas tracers, are found to be very bright toward IC 342's nucleus (Meier & Turner 2005). HC_3N(5–4) appears to be an excellent extragalactic probe of the dense, quiescent molecular gas component not yet involved in the current starburst.

To quantitatively compare star formation with dense gas, a SFR is derived from the 45 GHz continuum flux (spectral indices measured between 2 cm and 7 mm demonstrate that the vast majority of flux toward GMCs B and C is thermal bremsstrahlung). The SFR is then compared with M_{den} (Table 4) to estimate a dense gas star formation efficiency, $SFE_{den} = SFR(M_\odot\,yr^{-1})/M_{den}(M_\odot)$. Dense gas depletion timescales, $\tau_{den} = 1/SFE_{den}$, are also computed. In Table 4, the ratio of the observed Lyman continuum ionization rate (e.g., Meier & Turner 2001; Tsai et al. 2006, corrected for distance) to M_{den} derived from the LVG analysis is reported. Toward the non-starburst GMCs $N_{Lyc}/M_{den} \simeq (1.6\text{–}4.0) \times 10^{45}\,s^{-1}\,M_\odot^{-1}$, while toward GMC B this ratio is 10–30 times larger. If one adopts the conversion from N_{Lyc} to SFR of $10^{-53}\,M_\odot\,yr^{-1}\,s^{-1}$ (e.g., Kennicutt 1998), then SFE_{den} for the starburst is $\sim 4 \times 10^{-7}\,yr^{-1}$, or dense gas depletion times of $\tau_{den} \simeq 2$–3 Myr. This highly

enhanced SFE_{den} is a direct consequence of the faint HC_3N emission here. Even toward the non-starburst clouds SFE_{den} are $(1.6–4.0) \times 10^{-8}$ yr^{-1}. These efficiencies are sufficiently short that they imply dense gas consumption timescales that are non-negligible fractions of the expected GMC lifetimes.

The dense SFE is rather high across the nucleus, but the extreme value toward GMC B is remarkable. Meier & Turner (2001) argued that intense star formation is suppressed along the spiral arms being triggered when the inflowing molecular gas collides with the inner ring molecular gas. Therefore, it is reasonable that in a relative sense SFE_{den} is lower away from the central ring. However, this leaves unexplained why GMC B's SFE_{den} is so much larger than GMC C, though its positions at the arm/inner ring intersection is the same. We suggest that this is a sign of the evolution of star formation across the nucleus that is impacted by radiative and mechanical feedback *from within* the molecular cloud.

5.3. Destruction/Dispersal of Dense Gas with Starburst Age

A possible cause of the different SFE_{den} between GMC C and B is that we are observing the clouds at high enough spatial resolution to begin to identify the changing internal structure of the clouds in the presence of the starburst. Over the lifetime of a cloud SFEs vary. In the earliest stages of a star formation episode SFEs will appear low because elevated SFRs have yet to convert the bulk of the molecular material to stars. Toward the final stages of a GMC's evolution instantaneous SFEs appear to increase dramatically as the cloud clumps are consumed, destroyed, or dispersed. So observed instantaneous SFEs are expected to vary widely throughout the lifetime of an individual GMC and relative to lifetime averaged SFEs typically considered in extragalactic studies.

If starburst B is a few Myr more evolved than the other GMCs, especially the dynamical similar C, then we may be witnessing the consumption, dispersal, or destruction phase of the remaining dense clumps in the presence of the expanding H II region. The magnitude of the dense gas consumption times for B are indeed shorter than the lifetime of the GMC. Several lines of evidence suggest that the (weaker) star formation toward C2 may be at a somewhat earlier phase. These include less extended H II regions (e.g., Tsai et al. 2006), bright hot-core-like species CH_3OH (Meier & Turner 2005), $NH_3(6,6)$ (Montero-Castaño et al. 2006), and CO(6–5) (e.g., Harris et al. 1991), and more millimeter dust continuum emission (e.g., Meier & Turner 2001).

In this context, it is interesting to compare the thermal pressure of the starburst H II region with that of the dense clumps along the same line of sight. Assuming a Strömgren sphere of $R \sim 3$ pc, $N_{Lyc} = 1.1 \times 10^{51}$ s^{-1}, and $T_e = 8000$ K, parameters determined for the main starburst H II (Tsai et al. 2006), the thermal pressure of such an H II region would be $n_e T_e = 10^{6.76}$ cm^{-3} K. This value is equal given the uncertainties to $n_{H_2} T_K \simeq 10^{6.57}$–$10^{6.75}$ cm^{-3} K for the dense component of GMC B, hinting at pressure balance between the dense clumps and the H II region. In addition, the filling factor of the H II region is larger than implied by the HC_3N LVG analysis. So it is possible that HC_3N emission toward GMC B comes from dense clumps embedded within the H II region.

The above analysis suggests the following physical picture for the faint HC_3N emission toward the starburst. The starburst toward B is more evolved. The H II region at GMC B has had time to expand, destroying, or dispersing the dense gas, which is now in the form of smaller clumps and/or more diffuse gas. Clumps that remain there must have high pressure to survive. Near the younger star-forming cloud GMC C (particularly toward GMC C2), the H II regions may just be developing, and have not had time to disperse the clouds. The dense clumps here would be more abundant and still present a hot-core-like chemistry. The clouds further from the central are on average less dense and at the current epoch remain largely quiescent, except possibly D′, where the second high-excitation component could be associated with the presence of shocks (Meier & Turner 2005).

6. CONCLUSIONS

We have imaged the HC_3N $J = 5$–4 line in the nucleus of IC 342 with the VLA and the HC_3N(16–15) line with the PdBI at $\lesssim 2''$ resolution. These are the first maps of these transitions in an external galaxy. We have detected emission extended along the nuclear "mini-spiral" in (5–4) and more concentrated emission in (16–15), with relative abundance of $X(HC_3N) \sim 1 \times 10^{-9}$. HC_3N emission is not tightly correlated with star formation strength. Dense gas *excitation*, however, follows star formation more closely. GMC B, which is weak in all the HC_3N lines, is relatively stronger in the higher J lines.

LVG modeling indicates that the HC_3N-emitting gas has densities of 10^4–10^5 cm^{-3}. In IC 342, physical conditions of the densest component are fairly constant away from the immediate environment of the starburst, though beyond the central ring densities begin to fall. Comparison with the $C^{18}O$ observations of Meier & Turner (2001) reveals excitation temperatures similar to $C^{18}O$ values indicating either that the molecular gas is dense and cool ($T_k < 20$ K) or that there are multiple gas components where the densities and kinetic temperatures of each component conspire to give similar overall excitation. The strong overprediction of the amount of gas mass present, if densities are large and temperatures cool, favors a multi-component ISM with at least two components beside the diffuse one seen in ^{12}CO(2–1). The actual ISM is likely a continuum of cloud densities with different densities dominating different tracers. HC_3N also differs in morphology from HCN(1–0), with HCN(1–0) being much brighter toward the starburst. This is further evidence that there are multiple dense gas components.

Of particular interest, the starburst site (GMC B) exhibits the largest difference in intensity between HC_3N (both transitions) and HCN(1–0). The faintness of the HC_3N here suggests that the brightness of HCN(1–0) is not due solely to large quantities of dense gas. A comparison between the GMCs with the largest SFRs and similar dynamical environments, B and C, hint at an explanation. While GMC B shows higher excitation, the low brightness of this cloud indicates that it is composed of a relatively small amount of warm, dense clumps. The smaller amount of dense gas at the site of the strongest young star formation indicate high star formation efficiencies in the dense gas. Toward GMC C, HC_3N, CH_3OH, and NH_3 are more intense and the fraction of millimeter continuum from dust is higher. This indicates that GMC C is in an early, less evolved (hot-core-like) state. The extreme dense gas SFE observed toward GMC B reflects the fact that the main burst is in a more evolved state. The dense clumps toward the starburst are being dispersed or destroyed in the presence of the H II region. The little dense gas remaining appears to be in pressure equilibrium with the H II region. The larger opacity of HCN(1–0) relative to HC_3N elevates its brightness temperature in this warm gas and lowers its critical density permitting it to remain excited in the somewhat lower density component.

We conclude that EVLA observations of $HC_3N(5–4)$ can be a powerful probe of dense, quiescent molecular gas in galaxies, and when combined with high-resolution imaging of the higher J transitions of HC_3N with current and upcoming millimeter interferometers (like ALMA) provide tight constraints on dense molecular gas properties in stronger or more widespread starbursts, where changes like those localized to GMC B are expected to permeate much of the ISM.

We thank Chris Carilli and Miller Goss for assistance with the VLA observations. We also thank Philippe Salome and Nemesio Rodriguez for their help with the PdBI observations and data reduction. We thank the referee for several suggestions that improved the presentation. D.S.M. acknowledges support from the National Radio Astronomy Observatory which is operated by Associated Universities, Inc., under cooperative agreement with the National Science Foundation and NSF grant AST-1009620. This work is also supported by NSF grants AST-0307950 and AST-0506469 to J.L.T.

REFERENCES

Aalto, S., Polatidis, A. G., Hüttemeister, S., & Curran, S. J. 2002, A&A, 381, 783
Aladro, R., Martín-Pintado, J., Martín, S., Mauersberger, R., & Bayet, E. 2011, A&A, 525, A89
Becklin, E. E., Gatley, I., Mathews, K., Neugebauer, G., Sellgren, K., Werner, M. K., & Wynn-Williams, C. G. 1980, ApJ, 236, 441
Brandl, B. R., et al. 2006, ApJ, 653, 1129
Bussmann, R. S., et al. 2008, ApJ, 681, L73
Costagliola, F., & Aalto, S. 2010, A&A, 515, 71
Dahmen, G., Huttemeister, S., Wilson, T. L., & Mauersberger, R. 1998, A&A, 331, 959
de Vicente, P., Martín-Pintado, J., Neri, R., & Colom, P. 2000, A&A, 361, 1058
Downes, D., Radford, S. J. E., Giulloteau, S., Guelin, M., Greve, A., & Morris, D. 1992, A&A, 262, 424
Fuente, A., Martin-Pintado, J., Cernicharo, J., & Bachiller, R. 1993, A&A, 276, 473
Gao, Y., & Solomon, P. M. 2004, ApJ, 606, 271
García-Burillo, S., Martín-Pintado, J., Fuente, A., & Neri, R. 2000, A&A, 355, 499
García-Burillo, S., Martín-Pintado, J., Fuente, A., & Neri, R. 2001, ApJ, 563, L27
García-Burillo, S., Martín-Pintado, J., Fuente, A., Usero, A., & Neri, R. 2002, ApJ, 575, L55
Graciá-Carpio, J., García-Burillo, S., Planesas, P., Fuente, A., & Usero, A. 2008, A&A, 479, 703
Green, S., & Chapman, S. 1978, ApJS, 37, 169
Harris, A. I., Hills, R. E., Stutzki, J., Graf, U. U., Russell, A. G., & Genzel, R. 1991, ApJ, 382, L75
Harrison, A., Henkel, C., & Russell, A. 1999, MNRAS, 303, 157
Ho, P. T. P., Martin, R. N., & Ruf, K. 1982, A&A, 113, 155
Ishizuki, S., Kawabe, R., Ishiguro, M., Okumura, S. K., Morita, K.-I., Chikada, Y., & Kasuga, T. 1990, Nature, 344, 224
Karachentsev, I. D. 2005, AJ, 129, 178
Kennicutt, R. C., Jr. 1998, ARA&A, 36, 189
Knudsen, K. K., Walter, F., Weiss, A., Bolatto, A., Riechers, D. A., & Menten, K. 2007, ApJ, 666, 156
Krips, M., Neri, R., García-Burillo, S., Martín, S., Combes, F., Graciá-Carpio, J., & Eckart, A. 2008, ApJ, 677, 262
Lafferty, W. J., & Lovas, F. J. 1978, J. Phys. Chem. Ref. Data, 7, 441
Larson, R. B. 1981, MNRAS, 194, 809
Lo, K. Y., et al. 1984, ApJ, 282, L59
Maloney, P., & Black, J. H. 1988, ApJ, 325, 389
Mauersberger, R., Henkel, C., & Sage, L. J. 1990, A&A, 236, 63
Meier, D. S., & Turner, J. L. 2001, ApJ, 551, 687
Meier, D. S., & Turner, J. L. 2004, AJ, 127, 2069
Meier, D. S., & Turner, J. L. 2005, ApJ, 618, 259
Meier, D. S., Turner, J. L., & Hurt, R. L. 2000, ApJ, 531, 200
Meier, D. S., Turner, J. L., & Hurt, R. L. 2008, ApJ, 675, 281
Montero-Castaño, M., Herrnstein, R. M., & Ho, P. T. P. 2006, ApJ, 646, 919
Morris, M., Turner, B. E., Palmer, P., & Zuckerman, B. 1976, ApJ, 205, 82
Myers, P. C., & Benson, P. J. 1983, ApJ, 266, 309
Narayanan, D., Cox, T. J., Shirley, Y., Davé, R., Hernquist, L., & Walker, C. K. 2008, ApJ, 684, 996
Papadopoulos, P. P. 2007, ApJ, 656, 792
Rickard, L. J., & Harvey, P. M. 1984, AJ, 89, 1520
Saha, A., Claver, J., & Hoessel, J. G. 2002, AJ, 124, 839
Sakamoto, S. 1996, ApJ, 462, 215
Schinnerer, E., Böker, T., & Meier, D. S. 2003, ApJ, 591, L115
Schinnerer, E., Böker, T., Meier, D. S., & Calzetti, D. 2008, ApJ, 684, L21
Scoville, N. Z., & Sanders, D. B. 1987, in Interstellar Processes, ed. D. J. Hollenbach & H. A. Thronson, Jr. (Dordrecht: Reidel), 21
Scoville, N. Z., Yun, M. S., & Bryant, P. M. 1997, ApJ, 484, 702
Smith, P. A., Brand, P. W. J. L., Mountain, C. M., Puxley, P. J., & Nakai, N. 1991, MNRAS, 252, 6
Solomon, P. M., Rivolo, A. R., Barrett, J., & Yahil, A. 1987, ApJ, 319, 730
Stark, A. A., Bally, J., Wilson, R. W., & Pound, M. W. 1989, in The Center of the Galaxy, ed. M. Morris (Dordrecht: Kluwer), 129
Tsai, C.-W., Turner, J. L., Beck, S. C., Crosthwaite, L. P., Ho, P. T. P., & Meier, D. S. 2006, AJ, 132, 2383
Turner, J. L., & Ho, P. T. P. 1983, ApJ, 268, L79
Turner, J. L., & Hurt, R. L. 1992, ApJ, 384, 72
Turner, J. L., Hurt, R. L., & Hudson, D. Y. 1993, ApJ, 413, L19
Usero, A., García-Burillo, S., Fuente, A., Martín-Pintado, J., & Rodríguez-Fernández, N. J. 2004, A&A, 419, 897
Usero, A., García-Burillo, S., Martín-Pintado, J., Fuente, A., & Neri, R. 2006, A&A, 448, 457
Vanden Bout, P. A., Loren, R. B., Snell, R. L., & Wootten, A. 1983, ApJ, 271, 161
Wall, W. F. 2007, MNRAS, 379, 674
Wu, J., Evans, N. J., II, Gao, Y., Solomon, P. M., Shirley, Y. L., & Vanden Bout, P. A. 2005, ApJ, 635, L173
Zinchenko, I., Pirogov, L., & Toriseva, M. 1998, A&AS, 133, 337